Tissue characterization using high wave number Raman spectroscopy

S. Koljenović
T. C. Bakker Schut
R. Wolthuis
B. de Jong
Erasmus Medical Center
Center for Optical Diagnostics and Therapy
Rotterdam, The Netherlands

L. Santos
Erasmus Medical Center
Center for Optical Diagnostics and Therapy
Rotterdam, The Netherlands
  and
Instituto Superior Técnico
Departamento de Engenharia de Materiais
Lisbon, Portugal

P. J. Caspers
Erasmus Medical Center
Center for Optical Diagnostics and Therapy
Rotterdam, The Netherlands

J. M. Kros
Erasmus Medical Center
Department of Pathology
Rotterdam, The Netherlands

G. J. Puppels
Erasmus Medical Center
Center for Optical Diagnostics and Therapy
Rotterdam, The Netherlands

Abstract. Raman spectroscopy is a powerful diagnostic tool, enabling tissue identification and classification. Mostly, the so-called fingerprint ($\sim$400–1800 cm^{-1}) spectral region is used. *In vivo* application often requires small flexible fiber-optic probes, and is hindered by the intense Raman signal that is generated in the fused silica core of the fiber. This necessitates filtering of laser light, which is guided to the tissue, and of the scattered light collected from the tissue, leading to complex and expensive designs. Fused silica has no Raman signal in the high wave number region (2400–3800 cm^{-1}). This enables the use of a single unfiltered fiber to guide laser light to the tissue and to collect scattered light in this spectral region. We show, by means of a comparison of *in vitro* Raman microspectroscopic maps of thin tissue sections (brain tumors, bladder), measured both in the high wave number region and in the fingerprint region, that essentially the same diagnostic information is obtained in the two wave number regions. This suggests that for many clinical applications the technological hurdle of designing and constructing suitable fiber-optic probes may be eliminated by using the high wave number region and a simple piece of standard optical fiber. © *2005 Society of Photo-Optical Instrumentation Engineers.* [DOI: 10.1117/1.1922307]

1 Introduction

Raman spectroscopy is a nondestructive vibrational spectroscopic technique, based on inelastic scattering of light by the molecules in a sample. A Raman spectrum contains detailed information about the molecular composition, molecular structures, and molecular interactions in a tissue.[1] Because different types of tissue differ in their overall molecular composition, their Raman spectra will also be different, and can be used as tissue-specific spectroscopic fingerprints. Pathological changes in a tissue are also accompanied by changes in molecular composition, and are reflected in the tissue spectrum, which enables development of diagnostic tools based on Raman spectroscopy.

An increasing number of Raman studies is providing evidence for the possibility to characterize and identify a large variety of normal tissues, pre-malignant tissues and tumors.[2–10] *In vivo* application of Raman spectroscopy in most cases requires the use of a flexible light guiding device of small diameter, such that it can for instance be introduced in the working channel of an endoscope or inside a biopsy needle or biopsy forceps. The fiber-optic probe must guide light to the tissue under investigation, collect light that is scattered by the tissue, and transport this collected light from the tissue to a spectrum analysis device. Successful steps towards *in vivo* application of the technique, by means of fiber-optic probes have been reported, among others by Mahadevan-Jansen et al. who collected *in vivo* spectra from human cervical tissue for the clinical diagnosis of cervical precancers,[8] by Buschman et al. who obtained *in vivo* intravascular Raman spectra from arteries,[9] and by Bakker Schut et al. who reported on the *in vivo* detection of epithelial dysplasia in rat palate tissue.[10] More recently, the potential of near-infrared Raman spectroscopy using optical fiber probes for diagnosis of lung cancer[11] and for differentiation of colonic polyps during gastrointestinal endoscopy[12] has been demonstrated. Several different miniaturized fiber-optic probes have been designed and realized[13–15] some of which indeed enabled high quality *in vivo* Raman spectra to be obtained.

In all these studies, the spectral region between 400 and 2000 cm^{-1}, commonly referred to as the "fingerprint region," was employed. This is a logical choice because this spectral region is very rich in information. Many different molecular vibrations lead to Raman scattering in this part of the spectrum. In many cases bands can be assigned to specific mo-

Address all correspondence to Dr. G. J. Puppels, Erasmus MC, Center for Optical Diagnostics and Therapy, Dr. Molewaterplein 50, room Wk 310, 3015 GE, Rotterdam, The Netherlands; Tel: (31)(10) 408-7989; Fax: (31)(10) 408-7671; E-mail: g.puppels@erasmusmc.nl

lecular vibrations and or molecular species, much aiding the interpretation of the spectra in terms of biochemical composition of the tissue.

However, the actual implementation of conventional fingerprint Raman spectroscopy for clinical purposes is hampered by the fact that in the 400–2000 cm^{-1} spectral region, the materials of the optical fiber itself generate Raman signal, resulting in a strong signal background. Unless measures are taken to suppress this fiber Raman signal, it will be more intense than the tissue Raman signal by at least 1 or 2 orders of magnitude. Moreover, bending of the fiber leads to variations in the amount of signal obtained from the core, cladding and coating materials, which makes it difficult to correct the tissue spectra for this background signal, thereby further complicating signal analysis. For this reason it is necessary to use optical filters at or near the distal end of the fiber-optic probe to suppress these background signal contributions. Examples are the Visionex probes used by Buschman[9] and Bakker Schut[10] and the probe recently described by Motz et al.[13] In these probes one fiber guides laser light to the tissue. This fiber contains a narrow bandpass filter at or near the distal end of the fiber which only transmits the laser light but blocks Raman scattered light that has been generated in the fiber. This implies of course that this fiber cannot be used to collect Raman scattered light from the tissue. Therefore the probes comprise multiple signal collection fibers. To avoid generation of Raman scattered light in these fibers, the light, which is collected, is first filtered by a high pass filter, which blocks the laser wavelength.

The combination of requirements for optical filtering leads to complex designs of fiber-optic probes for conventional fingerprint Raman spectroscopy. The complexity makes it difficult to miniaturize fiber-optic probes, which is necessary for instance for intravascular use[9,13] or for intracerebral use (i.e., stereotactic brain biopsy) and to ensure reproducible performance.[16] Besides, it is difficult to keep probes flexible, which is of great importance for use in the auxiliary channel of an endoscope.[12] The complexity is also an obstacle to the production of such probes at a price that they can be used as disposables in hospitals. Moreover, signal intensity in the 400–2000 cm^{-1} is relatively low, which may necessitate long signal integration time making it impractical for clinical use.

It is clear that there is a need for simple and small fiber-optic probes for measuring tissue Raman spectra that circumvent the problems mentioned earlier.

The solution we are exploring is to use the high wave number (HWVN) region of the Raman spectrum (~2400–3800 cm^{-1}). In this spectral region most of the spectral features obtained from tissue are strongly overlapping CH-stretching vibrations in the region 2800–3050 cm^{-1},[1] OH-stretching vibrations (primarily due to water), which appear in the spectral interval 3100–3500 cm^{-1},[1] smaller signal contributions of SH-stretching vibrations 2500–2600 cm^{-1},[17] and NH-stretching vibrations between 3100 and 3500 cm^{-1}.[1] At first glance the information content appears to be in sharp contrast with the information that can be obtained in the fingerprint wave number region (400–2000 cm^{-1}). Therefore it needs to be established that clinically relevant information can be derived from the high wave number (e.g., to distinguish between normal tissue and tumor).

For *in vivo* applications the use of the HWVN region has a very important practical advantage over the fingerprint region. No Raman signal is generated in fused silica in this wave number region. This implies that it should be possible to turn a single unfiltered optical fiber with a fused silica core into an *in vivo* Raman fiber-optic probe, which guides laser light to the tissue and also collects the light that is scattered by the tissue. Added benefits are that the Raman signal in the HWVN region is generally much more intense than the fingerprint Raman signal and that because of the large Stokes shift a very simple filter, such as a color glass filter can be used for laser suppression in the signal detection path.

Few studies have reported on the use of HWVN Raman spectroscopy for tissue characterization. Recently, this spectral region was used to determine the water concentration in brain tissue[18] and in skin.[19] Very detailed information about the composition and compositional heterogeneity of atherosclerotic plaque has been obtained recording and analyzing Raman spectral maps of thin tissue cross sections using only the 2400–3800 cm^{-1} region of its Raman spectrum.[20] Here, we report the results of a number of Raman microspectroscopic mapping experiments on thin tissue sections of brain tumors and bladder tissue to show that in many cases HWVN Raman spectroscopy enables the same level of discrimination between different types of tissue, and provides the same clinically relevant information as Raman spectroscopy in the fingerprint region. In addition, the technical feasibility of obtaining tissue Raman spectra by a single fiber probe is illustrated by measurements on porcine brain tissue, using a simple Raman setup constructed in house.

2 Materials and Methods

2.1 *Human Tissue Samples*

Approval for this study was obtained from the Medical Ethics Review Board of the Erasmus University Medical Center Rotterdam. The tissue specimens used were from resection material obtained during surgical procedures at the Departments of Neurosurgery, General Surgery, and Urology of the Erasmus MC Rotterdam. An informed consent form was signed preoperatively by each patient after receiving an explanation of study protocol. Tissue samples that were used included two brain malignancies (one glioblastoma, one meningioma) and normal bladder tissue (acquired from two patients, with bladder cancer). After excision, human tissue samples were snap frozen by immersion in liquid nitrogen and stored at −80 °C. For Raman microscopic mapping experiments, these frozen samples were cut into 25-μm-thick sections with a microtome at −20 °C and placed onto calcium fluoride (CaF_2) microscope slides. Unfixed tissue sections were dried in ambient air and used without further treatment. In order to confirm whether tissue was normal or tumor and to identify different structures within the tissue specimens, 5-μm-thick adjacent sections were also obtained and stained with hematoxilin & eosin (H&E) for histopathological evaluation. Light-microscopic images of the unstained tissue sections revealed heterogeneity in tissue structure, which could be linked to the structural heterogeneity observed in the stained adjacent sections. This assessment was used to select tissue regions for Raman mapping. To provide a direct comparison of the Ra-

man mapping results with histology, the 25-μm-thick tissue sections were H&E stained as well, after the Raman mapping measurements were completed.

2.2 Porcine Brain Tissue

Using a single fiber-optic probe *ex vivo* HWVN Raman spectra of larger tissue specimens were obtained. For these experiments brain tissue was used, which was obtained from a 4 month old pig, which was sacrificed after another unrelated terminal medical experiment. The brain was cut at the transversal plane in several 10–15 mm thick slices, which were placed in a physiological NaCl solution (i.e., 0.9%). Raman measurements were performed directly, without further pretreatment of the sample.

2.3 Instrumentation

2.3.1 Raman microspectroscopic mapping

Raman spectra of unstained tissue sections were collected using 719 and 847 nm laser light from an argon-ion pumped titanium:sapphire laser system (Spectra Physics, Mountain View, CA). The Raman microspectrometer that was used in these experiments has been has been described in detail by van de Poll et al.[21]

Briefly, the setup consists of a microscope (DM-RXE, Leica, Cambridge, UK) coupled to a Raman spectrometer (System 100, Renishaw, Wotton under Edge, UK). Laser light was focused on the sample by a 80× near-infrared optimized microscope objective (Olympus MIR-plan 80×/0.75, Japan) with a working distance of approximately 1.6 mm. Scattered light was collected by the same objective, filtered by a chevron type laser suppression filter and then focused onto the core of an optical fiber, which guides the Raman scattered light into a modified Renishaw system 100 spectrometer. Raman signal was collected in the spectral interval from 400 to 1800 cm^{-1} and from 2400 to 3800 cm^{-1}, with a spectral resolution of 8 cm^{-1} for both wave number regions. Unstained cryosections (25 μm) of tissue were placed under the microscope objective on an motorized, computer controlled *XYZ*-sample stage (Leica DM STC, Cambridge, UK), which enabled automatic scanning of the sample. The laser light was focused below the surface of the tissue at such a depth that the signal intensity was maximized. For each mapping experiment the tissue area to be scanned and the scanning step size were chosen, thereby dividing up the area of interest into small square areas (hereafter termed Raman pixel). Spectra were obtained consecutively from each of these Raman pixels, the size of which varied between 25 (5×5) μm^2 and 900 (30×30) μm^2, for different measurements. Since the laser spot size is much smaller than the area of the Raman pixels, each pixel was scanned during signal collection, in order to obtain a spectrum that is representative for the tissue in the Raman pixel. The laser power on the tissue samples was about 50 mW in all experiments. Spectra were acquired using 10 s of signal collection time per Raman pixel.

Acquisition of Raman spectra and microscopic stage movement was controlled by the WiRE 1.2 software (Renishaw) running under Grams/32 Spectral Notebase Software (Galactic Industries Corp., Salem, NH). Raman mapping software was implemented in Array Basic (the internal software platform of Grams) and controlled the Leica microscope unit and the microscope stage.

2.3.2 Raman fiber-optic probe measurements

Ex vivo Raman spectra were obtained by a Raman setup utilizing a single optical fiber to illuminate the tissue and to collect the scattered light from the tissue. For purposes of illustration a Raman spectrum measurement of porcine brain is shown in this manuscript. It was collected using 719 nm laser light of 40 mW from an argon-ion pumped titanium:sapphire laser (Spectra-Physics, 3900 S) and a signal collection time of 10 s. The laser light was coupled into a common optical fiber (with a core diameter of 200 μm and core and cladding consisting of fused silica, 2 m in length, (AS200/220IRAN, FiberTech, Berlin, Germany) at the proximal end. Laser light was guided to the tissue at the distal end of the fiber. Here also scattered light was collected and guided back to the proximal end of the fiber. The wavelength shifted light emerging from the fiber was then reflected off of a dichroic filter (which transmitted the laser wavelength), and guided into a multichannel spectrometer where the HWVN Raman spectrum of the tissue was recorded. A manuscript describing the setup in detail is in preparation.[22]

2.4 Data Analysis

All Raman data were processed with software developed inhouse that operates in the Matlab environment (The MathWorks, Inc., Natick, MA) using the multivariate statistical analysis toolbox PLS-toolbox 2.0.0c (Eigenvector Research, Inc., Manson, WA).

2.4.1 Pretreatment of spectra

Following acquisition, all spectra (*in vitro* and *ex vivo*) were first calibrated using Raman calibration standards as described earlier.[23] Briefly, two Raman calibration standards with accurately known peak frequencies [4-acetamidophenol (3102.4, 3326.6 cm^{-1}) and cyclohexane (2666.4, 2852.9, 29383.3 cm^{-1})] and the emission lines of a neon and a neon-argon lamp were used for wave number calibration of the spectra. The emission spectrum of a calibrated tungsten band lamp was used to correct recorded Raman spectra for the wavelength-dependent signal detection efficiency of the setup.[23] Spikes due to cosmic ray events were removed from the spectra, and the background signal, from optical elements in the laser light delivery pathway was subtracted from the tissue Raman spectra.

Because almost all spectral signatures from lipids and proteins appear in the 2700–3100 cm^{-1} interval, this range was chosen for analysis of the Raman spectra.

2.4.2 Raman maps

Raman pseudocolor maps were constructed for each of the tissue sections, based on the spectral data set that was obtained and using multivariate statistical techniques.

To minimize the influence of any slowly varying fluorescence or background scatter in the spectra, which is noninformative, the first derivative of the spectra was taken (using the Savitzky–Golay method). The resulting spectra were subse-

quently scaled so that all the derivative spectra of a map had zero mean and unit standard deviation (autoscaling or standard normal variate scaling).[23]

To orthogonalize and reduce the number of parameters needed to represent the signal variance in the spectral data set and to find groups of spectra that have resembling spectral characteristics, Principal component analysis[24] (PCA) and K-means cluster analysis[25] (KCA) were performed, respectively. The PCA scores, accounting for 99.9% of the variance captured, served as input for KCA. KCA was used because it can easily handle the large amounts of data as obtained during Raman mapping experiments. The algorithm was initiated by allowing the user to choose the number of clusters. The criteria used to determine the number of clusters to be included in the analysis were that the final cluster-averaged spectra displayed meaningful spectral differences (i.e., above noise level) and that the clusters could be related to histologically distinct areas at gross microscopic overview of the tissue sections. A Raman spectrum presents the overall molecular composition of the measurement volume in the tissue, because all molecules in the measurement volume contribute to the Raman signal. Spectra that are highly similar, and therefore were obtained of tissue areas of very similar molecular composition, end up in the same clusters. The cluster-membership information was plotted as a pseudocolor map by assigning a color to each different cluster. Depending on the size of the selected area and mapping resolution, the number of pixels per Raman map varied from 1978 to 7744 pixels.

2.4.3 Reference spectra

Reference Raman spectra were obtained of the following commercially available compounds: glycogen (type II, G-8751, Sigma-Aldrich Chemie, Zwijndrecht, The Netherlands), deoxyribose nucleic acid (DNA) (D-1501, Sigma, St. Louis, MO), cholesterol palmitate (150680, ICN Biochemicals Inc., OH), cholesterol linoleate (C-0289, Sigma-Aldrich Chemie, Zwijndrecht, The Netherlands), collagen (predominantly type I, 160083, ICN Biochemicals Inc., OH), actin, (A-3653, Sigma-Aldrich Chemie, Zwijndrecht, The Netherlands), and triolein (T-7140, Sigma, St. Louis, MO). These compounds were used without further purification. DNA was dissolved in demineralized water (20 mg/mL).

2.4.4 Spectral modeling

A least-squares fitting procedure was performed to obtain information about the differences in chemical composition between various histological structures. The *in vitro* HWVN Raman spectra of individual histological structures were fitted with spectra obtained from surrounding tissue plus spectra of one or more pure compounds (i.e., glycogen, cholesterol palmitate, DNA, cholesterol linoleate, collagen, actin, and triolein). This (nonrestricted) fitting procedure resulted in positive or negative fit contributions of the reference spectra that point out higher or lower concentrations of the corresponding compounds in tissue structures that were compared. Relative scattering cross sections were not determined and therefore all fit contributions are presented as arbitrary units and not as weight percentages.

The presence of noise in the spectra obtained from tissue may influence the fit results. To estimate the uncertainty in the
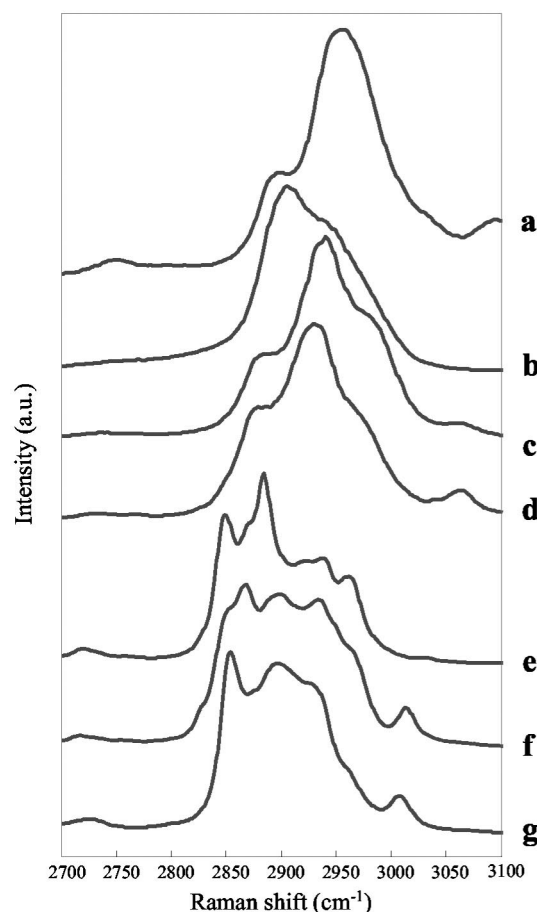
Fig. 1 HWVN Raman spectra of pure chemical compounds. (a) DNA, (b) glycogen, (c) collagen, (d) actin, (e) cholesterol palmitate, (f) cholesterol linoleate, (g) triolein.

fit results due to noise, artificial (normal distributed) noise was added to the tissue spectra that were fitted. In this way the signal-to-noise ratio of the tissue spectra was artificially decreased by a factor of 2. A new set of fit coefficients was calculated according to the last squares fitting procedure described earlier. This was repeated 100 times for each of the tissue spectra and the standard deviation obtained for each of the fit coefficients served as an estimate for the uncertainty in the fit results.

3 Results

3.1 HWVN Raman Spectra of Pure Compounds

HWVN Raman spectra from commercially available pure compounds (see Sec. 2), were obtained. Spectra are presented in Fig. 1.

3.2 Raman Mapping Experiments

3.2.1 Glioblastoma

Glioblastoma is the most malignant brain tumor. The diagnosis is based upon histopathological evaluation of tumor tissue samples, usually obtained by stereotactic surgery. It is essential that representative tissue is sampled, but this is made difficult by the facts that tumor tissue is highly heterogeneous,

while stereotactic biopsy samples are relatively small.[26] For example, an important histological parameter for establishing a diagnosis of glioblastoma is the presence of tumor necrosis.[26] When no necrotic tissue is sampled, it leads to underestimation of the tumor grade. On the other hand, histological diagnosis cannot be made when only necrotic tissue is present in the tissue sample.[26] An *in vitro* study has been published describing the potential of Raman spectroscopy for brain biopsy guidance. A classification model, based on spectra obtained in the fingerprint region, for discrimination between vital and necrotic tumor tissue yielded 100% accuracy.[5] In the fingerprint region it was shown that some of the most pronounced differences between vital and necrotic glioblastoma tissue were increased signal contributions of cholesterol and cholesterol esters in necrotic parts and increased levels of glycogen in vital tumor. In the present study these results served as guidance for the analysis of the HWVN spectra of glioblastoma vital and necrotic tissue. Later we show that HWVN spectra can also be used to discriminate between vital and necrotic tumor.

Panel A of Fig. 2 shows a bright field microscopic image of an unstained thin section of glioblastoma tissue, containing areas of necrosis and areas of vital tumor tissue. Panel B is a Raman map of the tissue section shown in panel A (7744 spectra, lateral resolution 20 μm). It was taken from our previous study on human glioblastoma tissue.[5] Red corresponds to vital tumor and blue corresponds to tumor necrosis (yellow represents the areas where no tissue is present). The map is based on a linear discriminant model developed on the basis of an extensive database of Raman spectra of vital glioblastoma tissue and of necrotic tissue, obtained in the 400–1800 cm^{-1} spectral region.[5] Panel C shows a Raman map of the same tissue section, but in this case based on a three-cluster KCA of Raman spectra obtained in the 2700–3100 cm^{-1} spectral region (7192 spectra, lateral resolution 21 μm). It is clear that a strong correlation exists between the necrotic and vital tissue areas identified in panel B and the result of the cluster analysis of the spectra obtained in the HWVN region. In HWVN Raman map (panel C) cluster 1 corresponds with vital tumor and cluster 2 with necrosis.

There are clearly significant differences between the cluster-averaged HWVN Raman spectra (Fig. 2, panel D). These spectral differences, pointing out a difference in chemical composition of vital and necrotic tumor tissue, were analyzed by a least-squares fit procedure. The average spectrum of the "vital cluster" [spectrum (a)] was fitted with a set of spectra consisting of the average of the "necrotic cluster" [spectrum (b)], and of the reference spectra obtained from DNA [see Fig. 1, spectrum (a)] and cholesterol palmitate [see Fig. 1, spectrum (e)]. In panel D, the fit-spectra of pure compounds (i.e., DNA and cholesterol palmitate) are shown after multiplication by the fit-coefficients that resulted from the least-squares fit [spectra (c) and (d)]. Therefore a positive or negative spectrum signifies that more or less of that compound is present in viable tumor than in necrotic tissue. The choice for these fit spectra was based on a first assessment of the shape of the difference spectrum between vital and necrotic tissue (not shown), on our earlier finding of higher cholesterol and cholesterol ester content of necrotic tissue[5] and on the disintegration of nuclei in necrotic tissue which can be expected to lead to lower DNA content. The small fit-residual

(e) suggests that this choice of fit spectra was justified. The fit results show that vital glioblastoma tissue has relatively stronger signal contributions from DNA but weaker signal from cholesterol esters (apparently cholesterol palmitate) when compared with necrotic tissue, in accordance with expectations.

Panels E and F show the result of a four-cluster KCA based on fingerprint spectra and HWVN Raman spectra, respectively, for the bottom part of the tissue section shown in panels A–C. The result is a subdivision of the vital tumor tissue into two clusters, which is a sign of heterogeneity in terms of molecular composition within the vital tumor, and which is very similar in both panels. Panel G shows the average spectra of clusters 1 [spectrum (a)] and 2 [spectrum (b)] of panel E and the spectrum of glycogen [spectrum (c)]. Comparison of these spectra makes clear that glycogen signal contributions (highlighted with gray bars) are much more prominent in spectrum (a). A multiple least-squares fit of spectrum (a) with spectra (b) and (c) resulted in the small fit residual shown by line (d). This makes clear that indeed the difference in glycogen content between the two vital tumor areas is the most prominent difference in molecular composition, although the presence of small spectral features in the fit residual does also point to other minor differences.

Panel H suggests that the biochemical ground for the KCA-result based on HWVN spectra is the same. Average spectra of two vital clusters from panel F are shown; spectrum (a) is the average spectrum of cluster 1, spectrum (b) the average spectrum of cluster 2. Spectrum (c) is their difference spectrum, shown five times enlarged, and calculated in such a way that only positive difference features are present. A comparison of this rather featureless spectrum with the spectrum of glycogen [spectrum (d)] shows great similarity. Spectrum (e) is the residual of a multiple least-squares fit of spectrum (a) with spectrum (b) and the glycogen spectrum. The fact that it is virtually a straight line suggests that also in the HWVN spectra it is the difference in glycogen signal intensity which separates the two vital tumor areas, although its spectral features are much less characteristic than in the fingerprint region.

The influence of noise, present in the tissue spectra, on the fit results was investigated for all of the fits presented earlier. Shot noise was artificially added to the average spectra of both the vital cluster and necrotic cluster [spectra (a) and (b) in panel D] and the averages of both the vital clusters from panels E and F [spectra (a) and (b) in panels G and H]. A new set of fit coefficients was calculated (see Sec. 2), which showed that spectral noise had very little influence on the fit results, indicating that it is of no consequence to the conclusions drawn on the basis of the fits (for the fit result presented in panel D calculated errors were: ~1% for the average of necrotic cluster, ~5 for DNA %, and ~6% for cholesterol palmitate; for both the fits shown in panels G and H errors were: ~1% for the average of vital cluster 2 and ~8% for glycogen).

3.2.2 *Meningioma*

Meningiomas are the most common benign tumors of central nervous system. They are rounded and usually attached to the dura. Although predominantly benign, these brain tumors
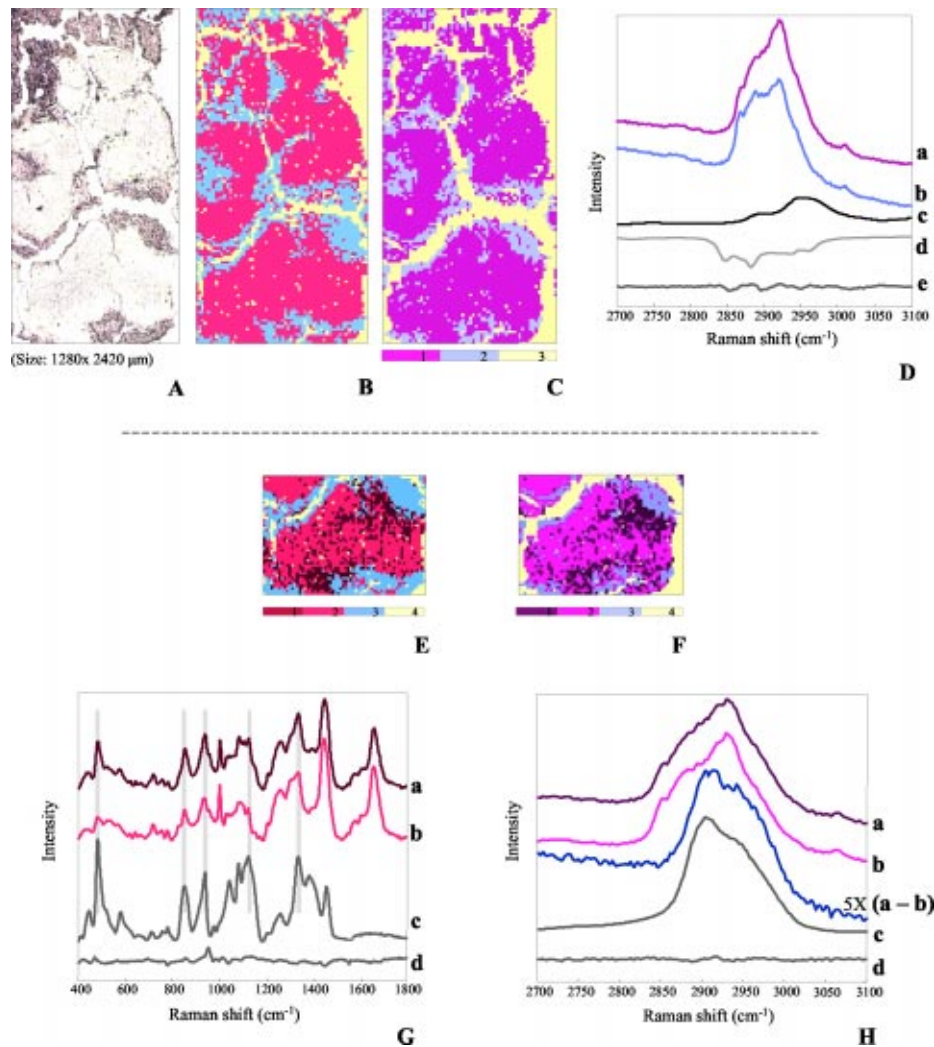
Fig. 2 Comparison of results from Raman experiments on glioblastoma in the fingerprint and HWVN spectral regions. Note: images shown in panels A and B are taken from Koljenović et al. (see Ref. 5). Panel A: Bright field photomicrograph of the unstained glioblastoma tissue section used for Raman microspectroscopic mapping (original magnification×5). Panel B: Raman map of the tissue section shown in panel A based on measurements in the fingerprint region (400–1900 cm^{-1}) and classification of each pixel as necrotic or vital on the basis of a linear discriminant analysis model (see Ref. 5) (pixel size 20×20 μm^2, 64×121 pixels). Panel C: Raman map of the tissue section shown in panel A, based on measurements in the high wave number region (2700–3100 cm^{-1}) and a K-means cluster analysis of the results (see text) (pixel size 21×21 μm^2, 62×116 pixels). Note the great correspondence with panel B. Red (cluster 1) indicates vital tumor and blue (cluster 2) indicates necrosis. Note: yellow (cluster 3) represents the areas in the scan where no tissue was present (edges, freezing artifacts). Panel D: Result of a least-squares fit analysis of the HWVN vital and necrotic tissue spectra. The average spectrum of vital tumor was fitted with the average spectrum of necrosis and the spectra of pure DNA (see Fig. 1) and of pure cholesterol palmitate (see Fig. 1). (a) Cluster-average of vital tumor; (b), (c), and (d) fit-spectra (necrosis, DNA, and cholesterol palmitate, respectively), which are shown after multiplication by the fit coefficients that resulted from the least-squares fit. A positive or negative spectrum signifies more or less of that compound is present in vital tumor than in necrosis; (e) fit-residual. (For clarity the spectra have been shifted along the ordinate.) Panels E and F: Fingerprint and HWVN Raman images demonstrating chemical heterogeneity within vital glioblastoma. These images are based on a KCA performed on the spectra from a small area selected from the larger Raman maps (lower 1/3 of Raman map in panels B and C). Note the division of the vital cluster (cluster 1 of panels B and C) in two subclusters (clusters 1 and 2). Cluster 3 is necrotic cluster. Panel G: Analysis of spectra obtained in the fingerprint region. The average spectrum of the "vital subcluster 1" was fitted with the spectrum of "vital subcluster 2" and the spectrum of pure glycogen. (a) Average spectrum of the vital subcluster 1, (b) average spectrum of vital subcluster 2, (c) spectrum of pure glycogen, (d) fit-residual. (The spectra have been shifted along the ordinate for clarity.) Panel H: Analysis of spectra obtained in the HWVN region. (a) and (b) Averages of two vital subclusters, clusters 1 and 2 of panel F, (a)–(b) positive difference spectrum of spectra a and b (a minus b), magnified by a factor of 5 for clarity, (d) spectrum of pure glycogen, (e) fit residual [resulting from fit of spectrum (a) by spectra (b) and (d)]. (For clarity the spectra have been shifted along the ordinate.)

often recur even after apparently complete resection.[27] Unfortunately, there are no per-operative tools to make sure whether or not all tumor tissue has been removed. The real extent of failure is therefore unknown until the tumor has grown significantly. *In vivo* HWVN Raman spectroscopic identification

of tumor cells attached to dura may be able to facilitate total tumor resection, resulting in decreased meningioma recurrence rates.

Figure 3 shows the results of a Raman mapping experiment on a thin section of human meningioma, microcystic
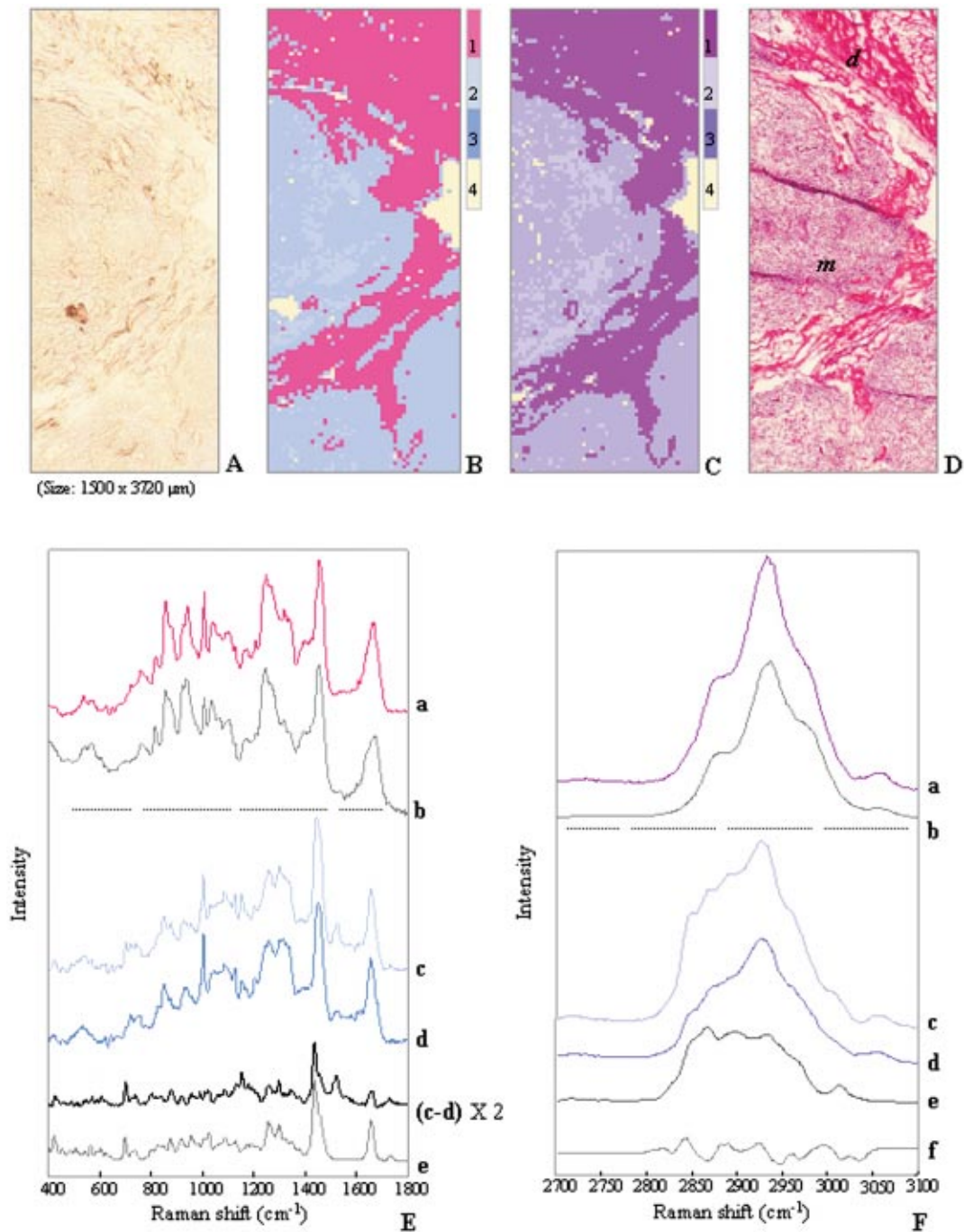
Fig. 3 Fingerprint and HWVN Raman microspectroscopic mapping experiments on unstained frozen tissue section containing dura and meningioma. Panel A: Photograph of unstained frozen section of tumor attached to dura (original magnification×5). Panel B: Pseudocolor Raman map of the tissue section shown in panel A, based on measurements in the fingerprint region (400–1800 cm^{-1}) and a *K*-means cluster analysis of the collected spectra (pixel size: 30×30 μm^2, 50×124 pixels). Panel C: Pseudocolor Raman map of the tissue section shown in panel A, based on measurements in the HWVN region (2700–3100 cm^{-1}) and a *K*-means cluster analysis of the collected spectra (pixel size: 30×30 μm^2, 51×127 pixels). It can be observed that the HWVN map closely resembles the fingerprint map. Panel D: Microscopic image of the tissue section of panel A after H&E staining. Dura is indicated with "*d*," meningioma with "*m*." As follows from a comparison of both Raman images with the image of the H&E stained tissue section, cluster 1 corresponds to dura and clusters 2 and 3 correspond to meningioma. (Cluster 4 represents the areas where no tissue was present in the section.) Panel E: Analysis of spectra obtained in the fingerprint region. (a) Average spectrum of dura; (b) spectrum of pure collagen. For clarity of presentation collagen spectrum was divided by factor 6; (c) and (d) averages from two meningioma clusters (clusters 2 and 3 in panel C); (c)–(d) positive difference spectrum of spectra (c) and (d) (c minus d), enlarged two times for clarity; (e) spectrum of pure cholesterol linoleate (divided by factor 3). Spectral regions of the most prominent resemblance are highlighted by gray bars. (For clarity the spectra have been shifted along the ordinate.) Panel F: Analysis of spectra obtained in the HWVN region. (a) Cluster-averaged spectrum of the dura (cluster 1 in panel C); (b) spectrum of pure collagen; (c) average spectrum of cluster 2 (represents the smaller part of meningioma in panel C), which was fitted with the average spectrum of cluster 3 (larger part of meningioma in panel C) and with the spectrum of pure cholesterol linoleate [see Fig. 1, spectrum (f)]; (d) and (e) fit-spectra (spectra of cluster 3 and of cholesterol linoleate, respectively) are shown after multiplication by the fit-coefficients that resulted from the least-squares fit; (f) fit-residual. (The spectra have been shifted along the ordinate for clarity.)

type, attached to dura. Raman spectra were obtained in both the fingerprint region (6200 spectra) and the HWVN region (6477 spectra), using a 30 μm lateral resolution. The area within the unstained tissue section that was selected for Raman mapping is shown in the bright field image in panel A. The fingerprint Raman image (panel B) and the HWVN Raman image (panel C), based on a four-cluster KCA are shown. The HWVN Raman image is virtually identical to the fingerprint Raman image, which indicates that the same clinical information can be obtained in both wave number regions. Comparison of these pseudocolor maps with the image of the tissue section after H&E staining (panel D) enabled identification of cluster 1 as dura (labeled "*d*" in panel D) and clusters 2 and 3 as meningioma (labeled "*m*" in panel D). Cluster 4 indicates the areas where no tissue is present.

The fingerprint cluster-averaged spectrum of dura [spectrum (a)] is shown in panel E. The dura is a tough fibrocollagenous layer mainly composed of fibroblasts and large amounts of collagen fibers.[28] This explains the strong similarity of the dura spectrum with the spectrum of pure collagen [spectrum (b)]. The averages of the meningioma clusters, clusters 2 and 3 [spectra (c) and (d), respectively], are also shown. Their difference spectrum [spectrum (c)–(d), two times enlarged] shows significant correspondence with the spectrum of pure cholesterol linoleate (e). This suggests that cholesterol (-esters) signal contributions (highlighted with gray bars) are much more prominent in average spectrum of the tumor area represented by cluster 2 than in that represented by cluster 3.

The same information can be obtained from the HWVN spectra. In panel F, cluster-averaged spectrum of dura (a) almost completely resembles the spectrum of collagen (b). The averaged spectrum of cluster 2 [spectrum (c), meningioma] was fitted with the average of cluster 3 [spectrum (d), meningioma] plus the spectrum of pure cholesterol linoleate [spectrum (e)]. The fit-spectra (d) and (e) are shown after multiplication by the fit coefficients that resulted from the least-squares fit. The fit residual is shown in spectrum (f). The fit residual is far from perfect, which indicates that there are other significant differences in molecular composition between different tumor regions than just differences in cholesterol ester content. Nevertheless, the fact that the spectrum of cholesterol linoleate significantly contributes to the fit, confirms the information obtained from fingerprint Raman spectra, that esterified cholesterol is one of the compounds that distinguishes different regions of meningioma. (Least squares fits including spectra of other compounds, such as free cholesterol and/or fatty acids did not improve the fit.) There is not much literature addressing the issue of the biochemical heterogeneity of microcystic meningiomas. Histologically this type of meningioma is characterized (among other features) by cells with foamy cytoplasm,[29] which may well contain lipids, including the cholesterol esters identified by Raman.

The lipid components of these vacuoles are represented by the cholesterol signal obtained by Raman spectra. From a practical point of view it is important that the clinical information, which is obtained in the HWVN-region matches the information, which is obtained in the fingerprint region. However, in this case, the actual biochemical basis for this clinical information is apparently not exactly the same in the two wave number regions.
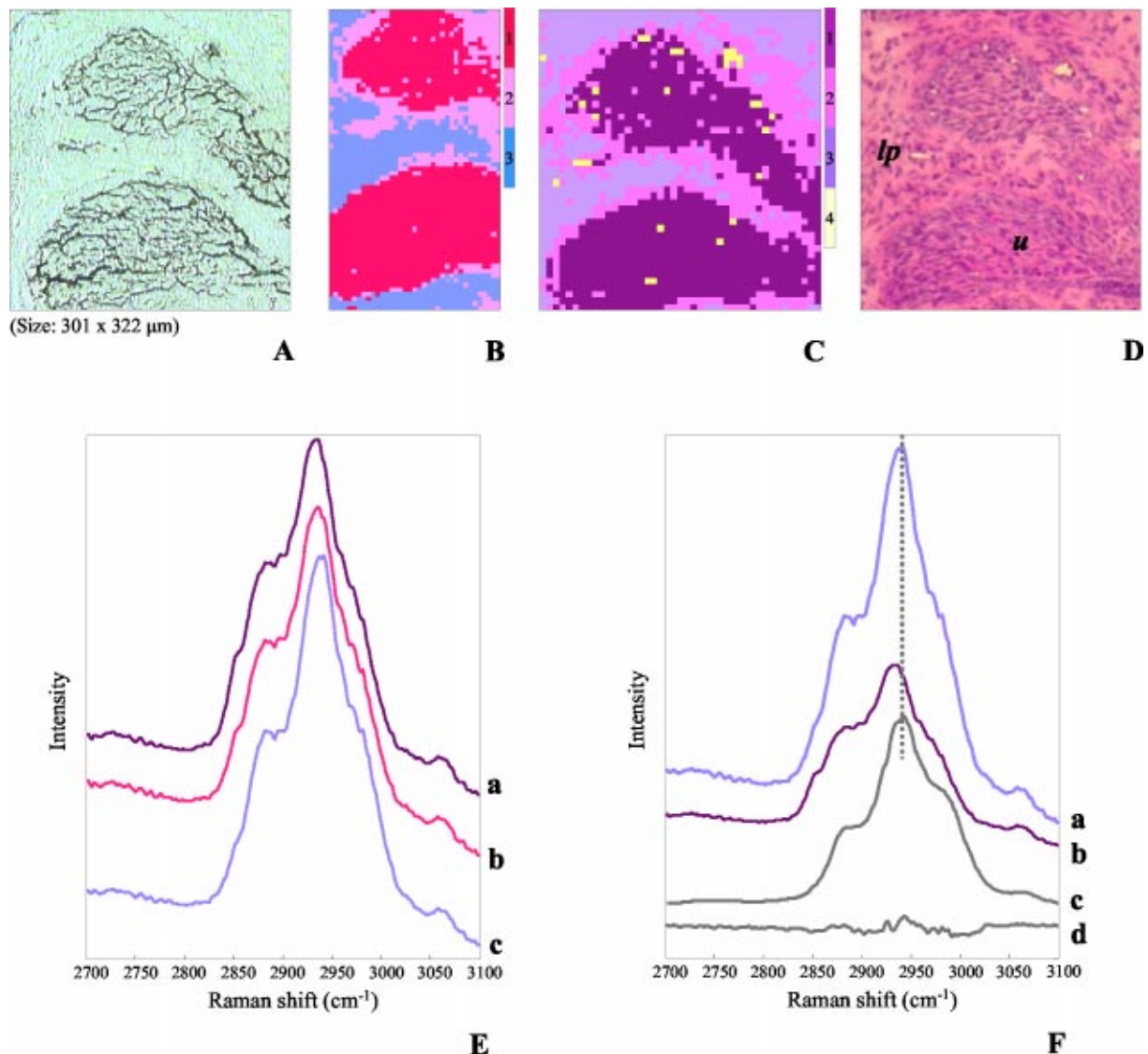
3.2.3 Bladder tissue

The result of a HWVN Raman mapping experiment carried out on a thin section of normal bladder tissue is displayed in Fig. 4. Panel A shows the unstained cryosection. Also on this tissue, a Raman mapping experiment was carried out using the fingerprint spectral region and the resulting Raman image (2405 spectra, lateral resolution 5 μm) is shown in panel B. Panel C shows the HWVN Raman map (1978 spectra, lateral resolution 7 μm). Again, the HWVN Raman image closely resembles the fingerprint Raman image. The Raman maps can be compared in the detail with the image of the same section after H&E staining in panel D ("*u*" indicates urothelium, "lp" indicates lamina propria). The urothelium (cluster 1) is clearly distinguishable from its supportive fibrocollagenous tissue (i.e., lamina propria, cluster 3), which is mainly composed of collagen.[28] The tissue area between urothelium and lamina propria is represented by cluster 2.

In panel E the average HWVN spectra of all tissue clusters are displayed. In the same way as described earlier for the other tissues, the characteristic HWVN spectral differences between the bladder urothelium and underlying lamina propria were analyzed by a least-squares fitting procedure. Panel F shows the fit residual (d) that remained after fitting the cluster-averaged spectrum obtained from lamina propria [cluster 3, spectrum (a)], with the average spectrum of urothelium cluster [spectrum (b) in panel E] and the spectrum obtained of pure collagen [see Fig. 1, spectrum (c)]. The fit-spectra (b) and (c) are shown after multiplication by the fit coefficients that resulted from the least-squares fit. Although the fit residual reveals some spectral features, there is still a strong indication that the lamina propria, in comparison with the bladder epithelium, has stronger signal contributions of collagen. Estimation of the influence of noise on the fit results (see Sec. 2) showed that also in this case it is negligible (noise-related uncertainty was ~1.3% for both the fit coefficients of urothelium and of collagen).

Figure 5 shows the result of HWVN Raman mapping experiment performed on unstained cryosection (panel A) of normal bladder tissue containing the submucosal region of fibrocollagenous tissue with bundles of smooth muscle, as was revealed by the adjacent H&E stained section. A total of 4620 Raman spectra were obtained with a lateral resolution of 7 μm and a three-cluster KCA was performed. In the resulting Raman pseudocolor map (panel B), which corresponds closely to the photograph of the unstained section, fibrocollagenous tissue is presented by cluster 1 and smooth muscle by cluster 3. The tissue area in between fibrocollagenous stroma and smooth muscle bundles is captured by cluster 2. The cluster average spectrum of this area can be almost completely reconstructed from the averages of clusters 1 and 3, using a least-squares fitting procedure (result not shown). This implies that in the terms of its chemical content, cluster 2 represents a transitional area between smooth muscle and its surrounding connective tissue. The HWVN cluster-average spectrum of smooth muscle [panel C, spectrum (a)], which is rich in myosin and actin,[28] was compared with the HWVN spectrum of pure actin [panel C, spectrum (b)]. It illustrates that the average of smooth muscle is dominated by the signal contributions of actin as emphasized with round dot line. Actin and myosin are major intracellular contractile proteins in

Fig. 4 Fingerprint and HWVN Raman microspectroscopic mapping experiment on normal bladder tissue. Panel A: photograph of an unstained bladder tissue section containing urothelium and underlying lamina propria (original magnification×10). Panel B: Pseudocolor Raman map of the bladder tissue section shown in panel A, based on measurements in the fingerprint region (400–1900 cm^{-1}) and a K-means cluster analysis of the collected spectra (pixel size: 5×5 μm^2, 37×65 pixels). Panel C: Pseudocolor Raman map of the bladder tissue section shown in panel A, based on measurements in the HWVN region (2700–3100 cm^{-1}) and a K-means cluster analysis of the collected spectra (pixel size: 7×7 μm^2, 43×46 pixels). Panel D: Photomicrograph of the tissue section of panel A after H&E staining. Panel E: Cluster-averaged HWVN Raman spectra calculated for the clusters obtained in panel C. (a) Urothelium, (b) area between urothelium and lamina propria, (c) lamina propria. Panel F: The result of a least-squares fitting procedure. The cluster-averaged spectrum collected from lamina propria was fitted with the cluster-averaged spectrum of urothelium (see original spectrum a in panel E) plus a spectrum of pure collagen [see Fig. 1, spectrum (c)]. (a) Average spectrum of lamina propria, (b) and (c) fit-spectra (cluster-averaged spectrum of urothelium and spectrum of pure collagen, respectively) shown after multiplication by their respective fit-coefficients, (d) fit-residual. (For clarity the spectra have been shifted along the ordinate.)

the muscle cells,[28] and their Raman spectra were found to be similar.[30] On the other hand, the HWVN cluster-average from fibrocollagenous tissue [panel C, spectrum (c)], which is rich in collagen,[28] was compared with the HWVN spectrum of pure collagen [panel C, spectrum (d)]. Collagen appears to be the main contributor in the spectrum of fibrocollagenous tissue as highlighted by solid line.

3.3 Ex vivo Raman Spectroscopy on Domestic Porcine Brain

Using a single fiber-optic probe a HWVN Raman spectrum of white matter from normal porcine brain was collected *ex vivo*.

Figure 6 shows the raw HWVN-spectrum [spectrum (a), including instrument signal background] and for comparison the same spectrum after correction for the background signal originating from instrument optics and the charge coupled device camera offset [spectrum (b)]. The background signal from the instrument is also shown [line (c)]. It can be observed that in the HWVN spectral region the instrument background signal is small compared to the tissue signal.

4   Discussion

The fingerprint region of the Raman spectrum has been used extensively for tissue characterization and tissue classifica-
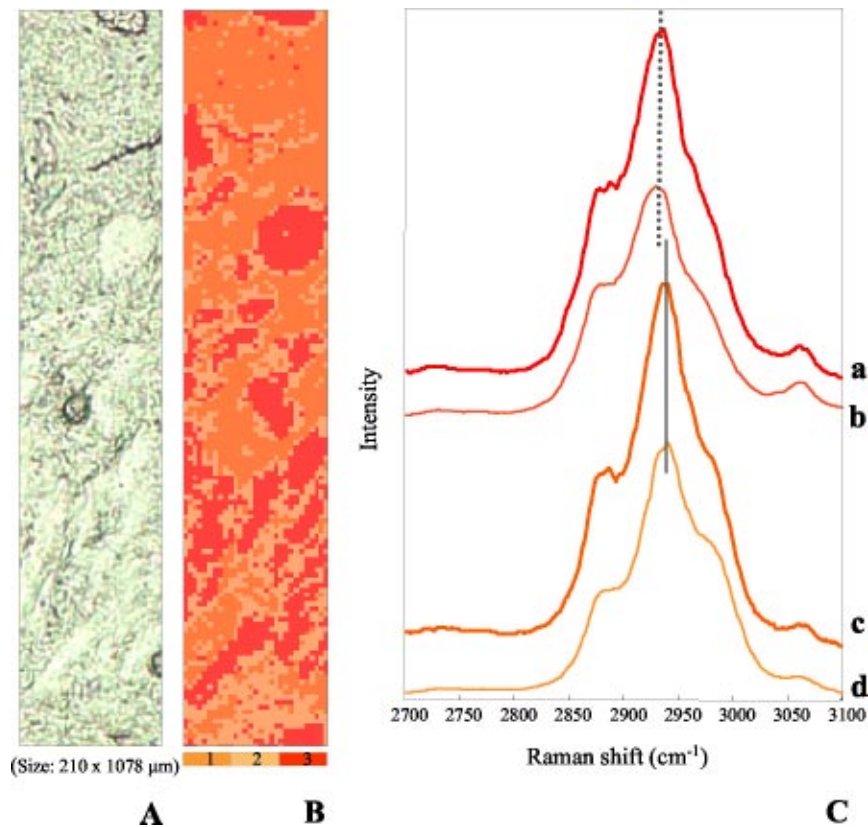
Fig. 5 HWVN Raman mapping experiment on normal bladder tissue containing fibrocollagenous stroma and smooth muscle tissue. Panel A: Photomicrograph of an unstained bladder tissue section containing fibrocollagenous stroma and smooth muscle tissue (original magnification×10). Panel B: Pseudocolor Raman map of the bladder tissue section shown in panel A, based on measurements in the HWVN region (2700–3100 cm^{-1}) and a K-means cluster analysis of the collected spectra (pixel size: 7×7 μm^2, 30×154 pixels). There is a clear co-localization of tissue structures visible in panel A and structures visible in the Raman map. The routine histological evaluation of adjacent H&E stained tissue section (not shown) revealed that cluster 1 of the Raman map represents fibrocollagenous tissue and that cluster 3 represents smooth muscle. The tissue area in between fibrocollagenous stroma and smooth muscle is captured by cluster 2. Panel C: (a) cluster-averaged spectrum of smooth muscle, (b) spectrum of pure actin, (c) cluster-averaged spectrum of fibrocollagenous stroma, (d) spectrum of pure collagen. (The spectra have been shifted along the ordinate for clarity.)

tion. This paper demonstrates the possibility to distinguish between different histological structures in a variety of tissues (glioblastoma, meningioma, and normal bladder tissue) based on Raman spectra obtained in the HWVN region.

This is an important finding since it means that clinically relevant information can be found in the HWVN region, which makes *in vivo* application of Raman spectroscopy by means of small and flexible fiber-optic probes much easier. In this wave number region the strong signal background from optical fibers, which is present in the fingerprint region is avoided.

The HWVN Raman pseudocolor maps presented here showed a high correspondence with spectral images recorded in fingerprint region on same unstained tissue sections. Therefore it appears that, just like fingerprint Raman spectra, HWVN Raman spectra contain sufficient information for tissue classification.

HWVN Raman spectra enable the discrimination of necrotic tissue from vital glioblastoma, because of the higher signal contributions of cholesterol esters in necrotic tumor tissue. The differences in the signal contributions of glycogen in the HWVN spectra from different regions of vital tumor illustrate the biochemical heterogeneity within the vital tumor.

These findings are supported by our earlier study on glioblastoma tissue using fingerprint spectral region.[5] The spectra also point to a relatively higher DNA content in vital glioblastoma. This is to be expected because of the disintegration of cell nuclei during necrosis. Large spectral differences exist between the HWVN Raman spectra of dura and meningioma, because of the high collagen content of dura. One of the most pronounced differences separating the HWVN spectra of different parts of the meningioma (microcystic type) is the signal contribution of cholesterol esters. This is in accordance with the information obtained from the fingerprint Raman spectra. The biochemical heterogeneity of the microcystic subtype of meningioma as revealed by Raman spectroscopy reflects the tumor areas in which the cells with the vacuolated cytoplasm, containing lipids including cholesterol, dominate.[29]

In normal bladder tissue sections HWVN Raman spectra also enable a clear distinction between bladder epithelium and underlying lamina propria, with again the strong signal contribution of collagen being a distinguishing hallmark of the lamina propria. The bundles of smooth muscle within the bladder wall were separated from their surrounding fibrocollagenous tissue by the stronger signal contribution of actin and the lower contribution of collagen. These results are in
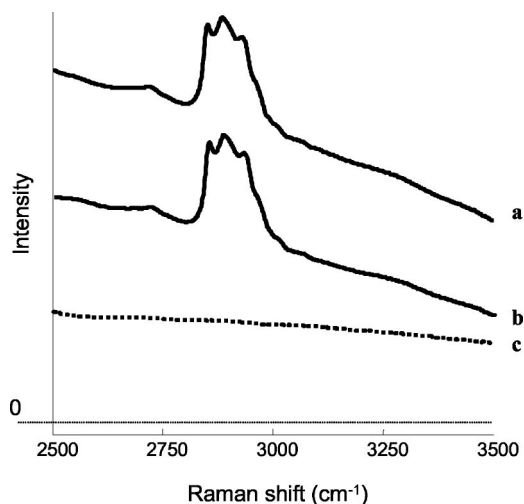
Fig. 6 Example of a HWVN Raman measurement of porcine brain tissue using a single fiber Raman probe. (a) Raw *ex vivo* HWVN Raman spectrum of white matter from porcine cerebellum tissue, (b) same spectrum after correction for the instrument background, (c) instrument background signal.

agreement with previous Raman spectroscopic studies of bladder wall in the fingerprint region of the Raman spectrum.[6]

Earlier studies, using a fiber-optic probe for measurements in the fingerprint region have already shown that real-time interpretation of *in vivo* spectra is possible.[16] This means that the feasibility of overcoming the technological hurdles that stand in the way of clinical implementation has been shown, which bodes well for the development of Raman guided clinical procedures and interventions, such as Raman guided biopsy and surgery.

References

1. A. T. Tu, *Basic Concept and Elementary Theory: Raman Spectroscopy in Biology*, Wiley, New York (1982).
2. C. J. Frank, D. C. B. Redd, T. S. Gansler, and R. L. McCreery, "Characterization of human breast biopsy specimens with Near-IR Raman spectroscopy," *Anal. Chem.* **66**, 319–326 (1994).
3. A. Mahadevan-Jansen, M. F. Mitchell, N. Ramanujam, A. Malpica, S. Thomasen, U. Utzinger, and R. Richards-Kortum, "Near-infrared Raman spectroscopy for *in vitro* detection of cervical precancers," *Photochem. Photobiol.* **68**, 123–132 (1998).
4. E. B. Hanlon, R. Manorahan, T. W. Koo, K. E. Shafer, J. T. Motz, M. Fitzmaurice, L. R. Kramer, I. Itzakan, R. R. Dasari, and M. S. Feld, "Prospects for *in vivo* Raman spectroscopy," *Phys. Med. Biol.* **45**, R1–R59 (2000).
5. S. Koljenović, L.-P. Choo-Smith, T. C. Bakker Schut, J. M. Kros, H. J. van den Berge, and G. J. Puppels, "Discriminating vital tumor from necrotic tissue in human glioblastoma tissue samples by Raman spectroscopy," *Lab. Invest.* **82**, 1265–1277 (2002).
6. B. W. D. de Jong, T. C. Bakker Schut, K. P. Wolffenbuttel, J. M. Nijman, D. J. Kok, and G. J. Puppels, "Identification of bladder wall layers by Raman spectroscopy," *J. Urol. (Baltimore)* **168**, 1771–1778 (2002).
7. J. Kneipp, T. C. Bakker Schut, M. Kliffen, M. Menke-Pluijmers, and G. J. Puppels, "Characterization of breast duct epithelia: a Raman spectroscopic study," *Vib. Spectrosc.* **32**, 67–74 (2003).
8. A. Mahadevan-Jansen, M. F. Mitchell, N. Ramanujam, U. Utzinger, and R. Richards-Kortum, "Development of a fiber optic probe to measure NIR Raman spectra of cervical tissue *in vivo*," *Photochem. Photobiol.* **68**, 427–431 (1998).
9. R. Buschman, E. T. Marple, M. L. Wach, B. Bennett, T. C. Bakker Schut, H. A. Bruining, A. V. Bruschke, A. van der Laarse, and G. J. Puppels, "*In vivo* determination of the molecular composition of artery wall by intravascular Raman spectroscopy," *Anal. Chem.* **72**, 3771–3775 (2000).
10. T. C. Bakker Schut, M. Witjes, M. Sterenborg, O. Speelman, J. Roodenburg, E. Marple, H. A. Bruining, and G. J. Puppels, "*In vivo* detection of dysplastic tissue by Raman spectroscopy," *Anal. Chem.* **72**, 6010–6018 (2002).
11. Z. Huang, A. McWilliams, H. Lui, D. McLean, D. I. S. Lam, and H. Zeng, "Near-infrared Raman spectroscopy for optical diagnosis of lung cancer," *Int. J. Cancer* **107**, 1047–1052 (2003).
12. A. Molckovsky, L.-M. Wong Kee Song, M. G. Shim, N. E. Marcon, and B. C. Wilson, "Dignostic potential of near-infrared Raman spectroscopy in the colon: differentiating adenomatous from hyperplastic polyps," *Gastrointest Endosc* **57**, 396–402 (2003).
13. J. T. Motz, M. Hunter, L. H. Galindo, J. A. Gradecki, J. R. Kramer, R. R. Dasari, and M. S. Feld, "Optical fiber probe for biomedical Raman spectroscopy," *Appl. Opt.* **43**, 542–554 (2004).
14. M. G. Shim, L. M. Song, N. E. Marcon, and B. C. Wilson, "*In vivo* near-infrared Raman spectroscopy," *Photochem. Photobiol.* **72**, 146–150 (2000).
15. G. J. Puppels, M. van Aken, R. Wolthuis, P. J. Caspers, T. C. Bakker Schut, H. A. Bruining, T. J. Romer, H. P. J. Buschman, M. Wach, and J. S. Robinson, "*In vivo* tissue characterization by Raman spectroscopy," *Proc. SPIE* **3257**, 78–85 (1998).
16. I. A. Boere, T. C. Bakker Schut, J. van den Boogert, R. W. F. de Bruin, and G. J. Puppels, *Vib. Spectrosc.* **32**, 47–55 (2003).
17. G. J. Thomas, Jr., "New structural insights from Raman spectroscopy of proteins and their assemblies," *Biopolymers* **67**, 214–225 (2002).
18. R. Wolthuis, M. van Aken, K. Fountas, J. S. Robinson, Jr., H. A. Bruining, and G. J. Puppels, "Determination of water concentration in brain tissue by Raman spectroscopy," *Anal. Chem.* **73**, 3915–3920 (2001).
19. P. J. Caspers, G. W. Lucassen, E. A. Carter, H. A. Bruining, and G. J. Puppels, "*In vivo* confocal Raman microspectroscopy of skin: non-invasive determination of molecular concentration profiles," *J. Invest. Dermatol.* **116**, 434–442 (2001).
20. S. W. E. van de Poll, A. Moelker, R. Wolthuis, T. C. Bakker Schut, S. Koljenović, A. van der Laarse, and G. J. Puppels, "Chemical characterization of atherosclerotic plaque by high-wavenumber Raman spectroscopy" (unpublished).
21. S. W. E. van de Poll, T. J. Romer, O. L. Volger, D. J. M. Delsing, T. C. Bakker Schut, H. M. G. Princen, J. W. Jukema, L. Havekes, A. van der Laarse, and G. J. Puppels, "Raman spectroscopic evaluation of the effects of diet and lipid-lowering therapy on athertosclerotic plaque development in mice," *Arterioscler. Thromb., Vasc. Biol.* **21**, 1630–1635 (2001).
22. L. F. Santos, R. Wolthuis, S. Koljenović, R. M. Almeida, and G. J. Puppels, "High wavenumber fiber-optic probes for *in vivo* Raman spectroscopy" (unpublished).
23. R. Wolthuis, T. C. Bakker Schut, P. J. Caspers, H. P. Buschman, T. J. Römer, H. A. Bruining, and G. J. Puppels, "Raman spectroscopic methods for *in vitro* and *in vivo* tissue characterization," in *Fluorescent and Luminescent Probes for Biological Activity*, W. T. Mason, Ed., Chap. 32, pp. 433–455, Academic, San Diego (1999).
24. I. T. Jollife, *Principal Component Analysis*, Springer, New York (1986).
25. A. K. Jain and R. C. Dubes, *Algorithms for Clustering Data*, Prentice Hall, Engelwood Cliffs, NJ (1988).
26. M. J. Glantz, P. Burger, J. Herndon, A. Friedman, J. Cairncross, N. Vick, and S. C. Schold, "Influence of the type of surgery on the histologic diagnosis in patients with anaplastic gliomas," *Neurology* **41**, 1741–1744 (1991).
27. H. Kamitani, H. Masuzawa, I. Kanazawa, and T. Kubo, "Recurrence of convexity meningiomas: tumor cells in the arachnoid membrane," *Surg. Neurol.* **56**, 228–235 (2001).
28. A. Stevens and J. Lowe, *Human Histology*, Times Mirror International, London (1997).
29. J. M. Bruner, R. D. Tien, and D. S. Enterline, "Tumors of the meninges and related tissues," in *Russell and Rubinstein's Pathology of Tumors of the Nervous System*, D. D. Bigner, R. E. McLendon, and J. M. Bruner, Eds., Chap. 11, pp. 69–139, Oxford University Press, New York (1998).
30. E. B. Carew, H. E. Stanley, J. C. Seidel, and J. Gergely, "Studies of myosin and its' proteolytic fragments by laser Raman spectroscopy," *Biophys. J.* **44**, 219–224 (1983).